Arabian Journal for Science and Engineering (2023) 48:3009–3019
https://doi.org/10.1007/s13369-022-07051-6

RESEARCH ARTICLE-MECHANICAL ENGINEERING

Mechanical and Microstructural Analysis of Exfoliated Graphite Nanoplatelets-Reinforced Aluminum Matrix Composites Synthesized via Friction Stir Processing

Xiaofeng Yu[1] · Wenbiao Gong[1] · Hua Wu[1] · Lili Duan[1]

Received: 24 February 2022 / Accepted: 9 June 2022 / Published online: 21 July 2022

Abstract
In this work, an investigation was conducted into the microstructure and mechanical characteristics of friction stir processed aluminum matrix composites (AMCs) reinforced with exfoliated graphite nanoplatelets (xGnPs). The microstructure was characterized using X-ray diffraction (XRD), electron backscattered diffraction (EBSD) and transmission electron microscopy (TEM), respectively. In addition, microhardness and tensile tests were performed to evaluate the differentiation of mechanical properties for all the samples. Field emission scanning electron microscopy was employed to reveal the fractographic features of all the samples. The results illustrated that the grains of the AMCs consist of equiaxed crystals with an average grain size of 3.2 μm, forming an ultrafine-grained microstructure. Additionally, the ratio of high angle grain boundaries in AMCs was higher than that of FSPed sample. The mechanical performance of AMCs was improved significantly as a result of Al_4C_3 generated in the solid-phase chemical reaction between the xGnPs and the Al matrix during FSP in combination with the fine grain strengthening. The microhardness, yield strength and ultimate tensile strength of AMCs reached 80 HV, 110 MPa and 210 MPa, respectively, which were 47, 69 and 20% higher than those of the base metal, respectively. The preferred orientation of the base metal transformed from < 200 > toward < 111 > , < 220 > and < 311 > owing to the combination effect of FSP and xGnPs. The incorporation of xGnPs ameliorated the mechanical properties of the AMCs dramatically, and the fracture surface of the AMCs was indicative of a combined ductile–brittle failure behavior.

Keywords Friction stir processing · Aluminum/xGnPs composite · Texture coefficient · Solid-phase chemical reaction · Mechanical performance

1 Introduction

Possessing phenomenal mechanical and physical performance, metal matrix composites could be regarded as one of the versatile materials that can be tailored to meet different industrial needs. To design and develop these materials, the processing technologies have involved advanced methods and characterized techniques in materials science and engineering. Since aluminum and its alloys possess excellent properties such as high specific strength, low density, distinguished corrosion resistance, workability and weldability, they provide promising applications in a wide range of areas from electronic packaging, aeronautical, aerospace and automotive [1–6]. Although aluminum alloys are extensively utilized in a variety of industries, the applications are restricted because their hardness, wear and corrosion resistances are lower than stainless steel materials [7]. It is a potential method to refine the grain and to handicap dislocation sliding through the incorporation of secondary phase particulate into Al matrix for enhancing the mechanical performance of aluminum alloys [8]. Powder metallurgy and molten metal technology are the main methods to prepare composites, in addition to the severe plastic deformation (SPD) techniques developed in recent years. There are several techniques introduced including pressurized squeeze casting

✉ Wenbiao Gong
gwbiao@163.com

✉ Hua Wu
wuhua@ccut.edu.cn

[1] Key Laboratory of Advanced Structural Materials of Ministry of Education, Changchun University of Technology, No. 2055 Street Yanan, District Chaoyang, Changchun 130012, People's Republic of China

Table 1 Chemical composition of 5052 alloy (wt%)

Al	Mg	Fe	Si	Cr	Mn	Cu
Base	2.21	0.291	0.2	0.147	0.113	0.0065

[9], accumulative roll bonding (ARB) and mechanical alloying (MA) [10, 11].

Evolving from friction stir welding (FSW) [12, 13], FSP has been effectively employed in the manufacture of metal matrix composites [14]. FSP is a thermo-mechanical solid state manufacturing technique where the material undergoes severe plastic deformation, heating and mixing. The heat is primarily generated from friction and plastic deformation [15]. Numerous academics have fabricated metal matrix composites successfully via FSP. Khodabakhshi et al. produced the aluminum matrix composites reinforced with nano-SiC particulates by FSP, and revealed that the textural components are comprised of the Goss/Cubic and P1/P2 dominant fiber components as a result of the incorporation of nano-particles [16]. By mixing flake graphite with aluminum powder and filled the grooves of aluminum plates, Mahdi Alishavandi et al. ameliorated strength-ductility efficiency of multi-layer graphene-reinforced aluminum composites through seven passes FSP, and discovered that the flake graphite was exfoliated in situ to a multilayer graphene sheet with a thickness of approximately 6 nm [17]. Kheirkhah et al. developed BN-reinforced Al matrix composites, and obtained the results indicating that the hardness, the yield strength (σ_y), tensile strength (σ_{UTS}) and elongation (%E) of specimens increased with an increase in the number of FSP passes [6]. Yijun Liu et al. successfully fabricated in situ exfoliated graphene/Al composites using Al2024 alloy as the substrate and nano-graphite as the reinforcing phase after four passes FSP and found that the hardness and electrical conductivity were significantly ameliorated compared to the specimens without the addition of nano-graphite [18]. Vikram Kumar S. Jain et al. developed Al5083-CNTs/SiC composites successfully through FSP processing and found out that CNT partially reacted with the Al5083 matrix to generate in situ Al_4C_3 intermetallic compound [19].

However, as far as the authors' knowledge, there are still few reports on the incorporation of xGnPs as a reinforcement into Al matrix via FSP to fabricate composites. Therefore, the objective of this work is to fabricate AMCs via FSP and evaluate the effect of the incorporation of xGnPs on the improvement of the microstructure and mechanical performance of the prepared composites systematically. Meanwhile, the stability of xGnPs during FSP processing has also been investigated.

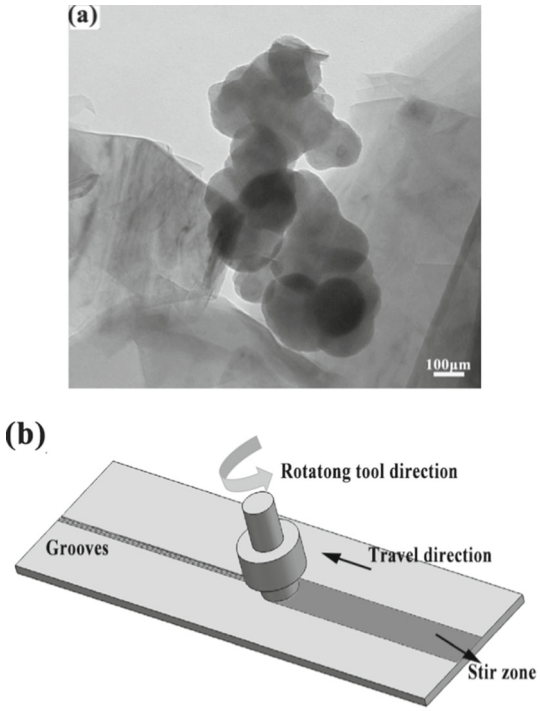

Fig. 1 **a** TEM image of the exfoliated graphite nanoplatelets, **b** schematic diagram for the preparation of AMCs

2 Materials and Experimental Procedure

2.1 Materials and Processing

In the present research, AA5052-O alloy sheet was utilized as base metal (BM) with a thickness of 5 mm, which was cross-sectioned to pieces with dimensions of 250 × 75mm^2. Table 1 shows the chemical composition of the AA5052-O alloy. The reinforcement particles were xGnPs, and the TEM image is shown in Fig. 1a. The schematic for the preparation of AMCs is shown in Fig. 1b. Initially, referring to the literature [20], two grooves were machined in the middle of the sheet to stow with xGnPs. The grooves dimensions and theoretical volume of xGnPs are depicted in Table 2. The processing was conducted by using a cylindrical tool with a shoulder diameter of 18 mm, and a threaded pin with a 6 mm width and a 3 mm height made from H13 steel. In order to achieve sufficient material flow with fewer FSP passes, the final processing parameters were determined with reference to the literature [19, 21]. FSP was carried out using a robotic FSW machine (FSW-LM-AL-16-2D) with a rotational speed

Table 2 Dimensions of the grooves and the theoretical volume of xGnPs

Dimension (mm)			Number of grooves	Intervals (mm)	Total volume of xGnPs (mm^3)	Synthesized AMCs volume (mm^3)
Width	Depth	Length				
1	1	250	2	1	500	5500

of 1400 rpm, a traverse speed of 50 mm/min, a counterclockwise rotational direction and a tool tilt angle of 2.5° for three cumulative FSP passes with 100% overlap to incorporate the embedded xGnPs properly. Additionally, aluminum matrix composites reinforced with xGnPs were denoted as AMCs. For comparison, BM was processed under the identical conditions without introducing any reinforcing powder, and the sample was nominated as FSPed Sample.

2.2 Characterization

The microstructure was etched using a modified Poulton's chemical reagent produced by mixing two chemical solutions: 1 mL H_2O–6 mL HNO_3–1 mL HF–12 mL HCl and 25 mL HNO_3–10 mL H_2O–1 g CrO_3. Optical microscope was employed to detect the cross section macrostructure of the AMCs. All of the samples were analyzed using XRD (Model: Rigaku D/ max 2500 diffractometer) with Cukα in the range of 20–90° at a rate of 2°/ min working at 40 mA and 100 kV. In order to further estimate the variation on the crystal structure of the samples after FSP, the texture coefficient was calculated using Eq. (1) developed by Berube and L' Esperance [22–24] for characterizing the preferred degree of different crystal planes.

$$T_c = \left(I_{(hkl)} / \sum_{i=1}^{n} I_{(hkl)} \right) \times \left(\sum_{i=1}^{n} I_{0(hkl)} / I_{0(hkl)} \right) \times 100 \quad (1)$$

where T_c represents texture coefficient, $I_{(hkl)}$ indicates the diffraction peak intensity of the (*hkl*) reflection of aluminum, $\sum I_{(hkl)}$ denotes the sum of the intensities for all the diffraction peaks monitored, and n is the number of peaks. The index 0 refers to the peak intensity of the standard Al powder sample, take from JCPDS file card number 85-1327. The orientation of the crystal planes conforms to random distribution when the texture coefficients are equal, whereas there is a preferred orientation of that crystal plane when the texture coefficient of a particular crystal plane is larger than the average. Furthermore, the preferred degree of the crystal plane is proportional to the texture coefficient. In this paper, the value of n is set to 4, i.e., the (111) (200) (220) and (311) crystal planes are taken for calculation, so that the crystal plane with a texture coefficient larger than 25% is regarded as the preferred orientation crystal plane.

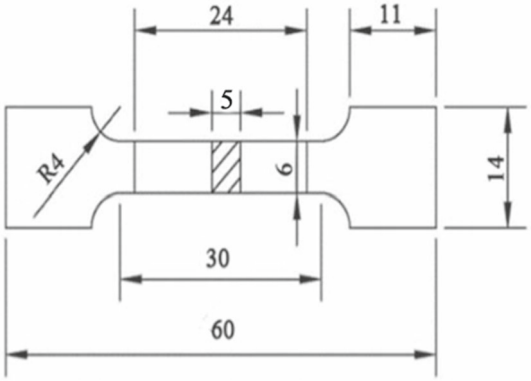

Fig. 2 Dimension of the tensile specimen

The structural information of xGnPs in AMCs was evaluated using a microscopic laser Raman spectrometer (LabRAM HR). Additionally, EBSD and TEM tests were performed to further characterize the specimens.

2.3 Evaluation of Mechanical Performance

Microhardness and tensile tests were carried out to determine the mechanical performance of all the samples. Microhardness was measured across the thickness section along a transverse line 2 mm below the top surface at an interval of 0.5 mm by microhardness tester (model:FM700), a load of 50 g and a 15 s dwell time. The tensile specimens were machined in terms of the schematic sketch, as shown in Fig. 2. Tensile tests were conducted at room temperature using a WDW-200 universal testing machine at a strain rate of 1 mm/min. The fracture surfaces of the investigated materials were evaluated using field emission scanning electron microscopy after tensile test.

3 Results and Discussion

3.1 Materials Flow Pattern

The morphology of local macrostructure from the stereographic cross section of the AMCs is shown in Fig. 3. It can be seen from the figure that there are no obvious macroscopic defects, such as voids and large agglomerations of xGnPs powder in the stir zone after FSP. It was determined that

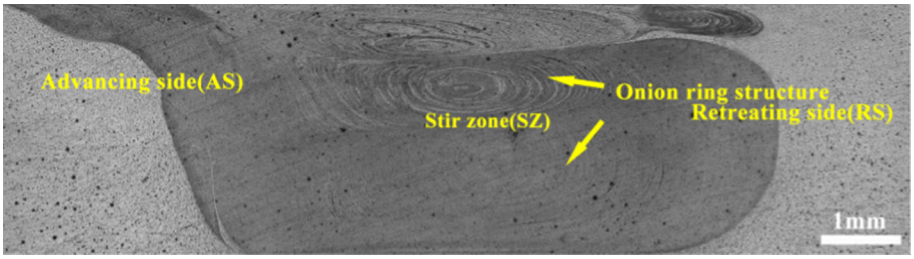

Fig. 3 Local stereographic macro-image from the thickness cross section of the AMCs

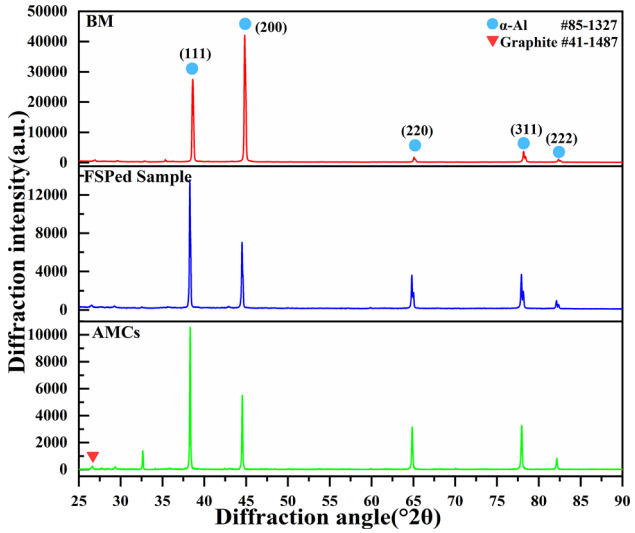

Fig. 4 XRD patterns of BM, FSPed sample and AMCs

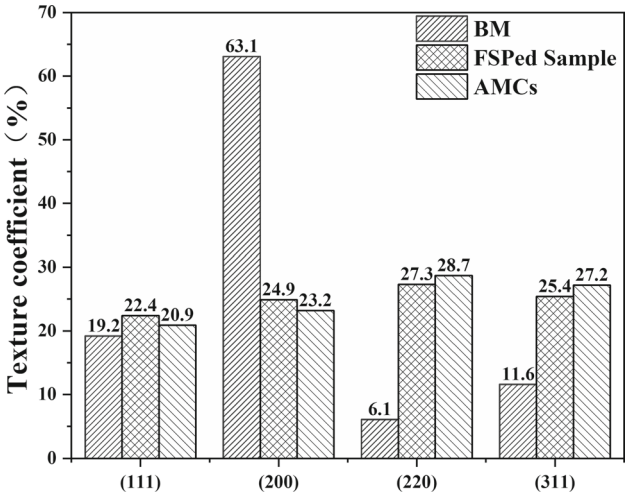

Fig. 5 Texture coefficients for BM, FSPed sample and AMCs

FSP could be employed to fabricate Al/xGnPs composites with excellent formation. According to the contrast arising from the xGnPs distribution after chemical etch, the material flow could be discriminated easily. It could be noticed that trapezoidal stir zone and onion ring structure were formed during FSP. The volume of the synthesized AMCs volume could be estimated from the area of the trapezoidal stir zone, as shown in Table 2. The profile of the onion ring structure could be regarded as a vortex swirl zone. It has been proposed that the formation of onion ring structure is ascribed to the convectional material flow during friction stirring before consolidation process, leading to the development of an elliptical texture across the thickness section of SZ from bottom to up primarily due to the effect of the rotating shoulder.

3.2 XRD Analysis

The X-ray diffractograms of all the samples are shown in Fig. 4. It could be found that there is a xGnP diffraction peak at $2\theta = 26.6°$ in AMCs. By combining the effect of FSP and xGnPs, it can be observed that the intensity of the diffraction peaks corresponding to the different crystal planes changed significantly.

Figure 5 shows the bar chart of texture coefficients for all the samples. BM shows a preferred orientation at < 200 > with a texture coefficient of 63.1%, suggesting the distinctive characteristic of rolling. In comparison with BM, the texture coefficient for FSPed sample decreases drastically, while that for (111), (220) and (311) increases significantly, which indicates that FSP is conducive to the growth of (111), (220) and (311), retarding the texture developed at < 200 > . Compared with FSPed sample, the texture coefficient of AMCs shows a slight increase in the crystal planes (111), (220) and (311), indicating that the preferred orientation is changed by not only FSP but also the addition of xGnPs particulates, promoting the development of the crystal planes (111), (220) and (311). Also, the increased texture coefficient of the (111) crystal plane contributes to the improvement of mechanical properties since crystal plane (111) is a densely packed surface of aluminum metal.

3.3 Microstructural Evolution

Figure 6 shows the grain structure of all the samples and the grain-size distribution of samples after FSP. BM is comprised of elongated grains parallel to the rolling direction, as shown in Fig. 6a. Moreover, the EBSD map from FSPed sample

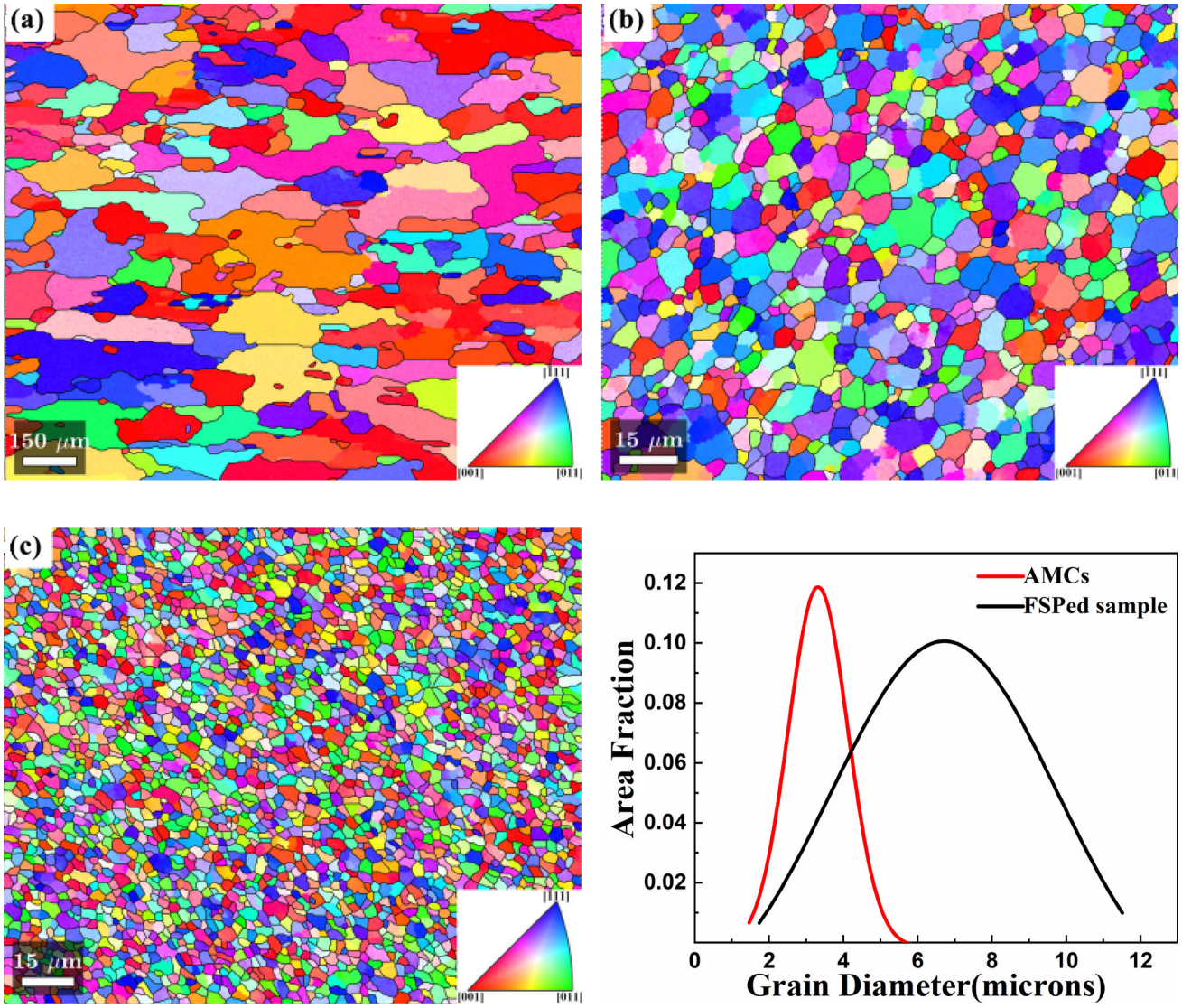

Fig. 6 EBSD images showing the grain structure of **a** the BM, **b** FSPed sample and **c** AMCs; **d** the grain size distribution of FSPed sample and AMCs

without incorporation of xGnPs reveals that an equiaxed bimodal fine grain structure was formed after FSP, and that the mean grain size was reduced from 147 μm of BM to about 7.1 μm of FSPed sample, which could ascribe to the thermo-mechanical effect generated from FSP processing and the generation of dynamic recrystallization (DRX) mechanism during FSP. Compared with FSPed sample, the equiaxed grain microstructure of AMCs was refined to about 3.2 μm, and grain orientation was randomly distributed, as shown in Fig. 6c. Meanwhile, as shown in Fig. 6d, the distribution profile of grain size in AMCs is remarkably narrower than that of the FSPed sample, suggesting that the addition of xGnPs can lead to a more uniform grain size, which may be related to the effect of xGnPs on the DRX process.

The main mechanisms involved in the FSP process comprise of dynamic recovery (DRV), continuous dynamic recrystallization (CDRX), discontinuous dynamic recrystallization (DDRX), geometric dynamic recrystallization (GDRX) as well as meta-dynamic recrystallization (MDRX) [25]. At the initial stage of deformation, there is an occurrence of multiplication and interaction of dislocation during DRV process in high stacking fault metals, such as aluminum, which gives rise to the formation of low angle grain boundaries [26]. Additionally, the degree of DRV increases with the more application of plastic strain, and high angle grain boundaries are formed owing to the transformation and annihilation of low angle grain boundaries, resulting in the appearance of CDRX. The strain-free grain with high

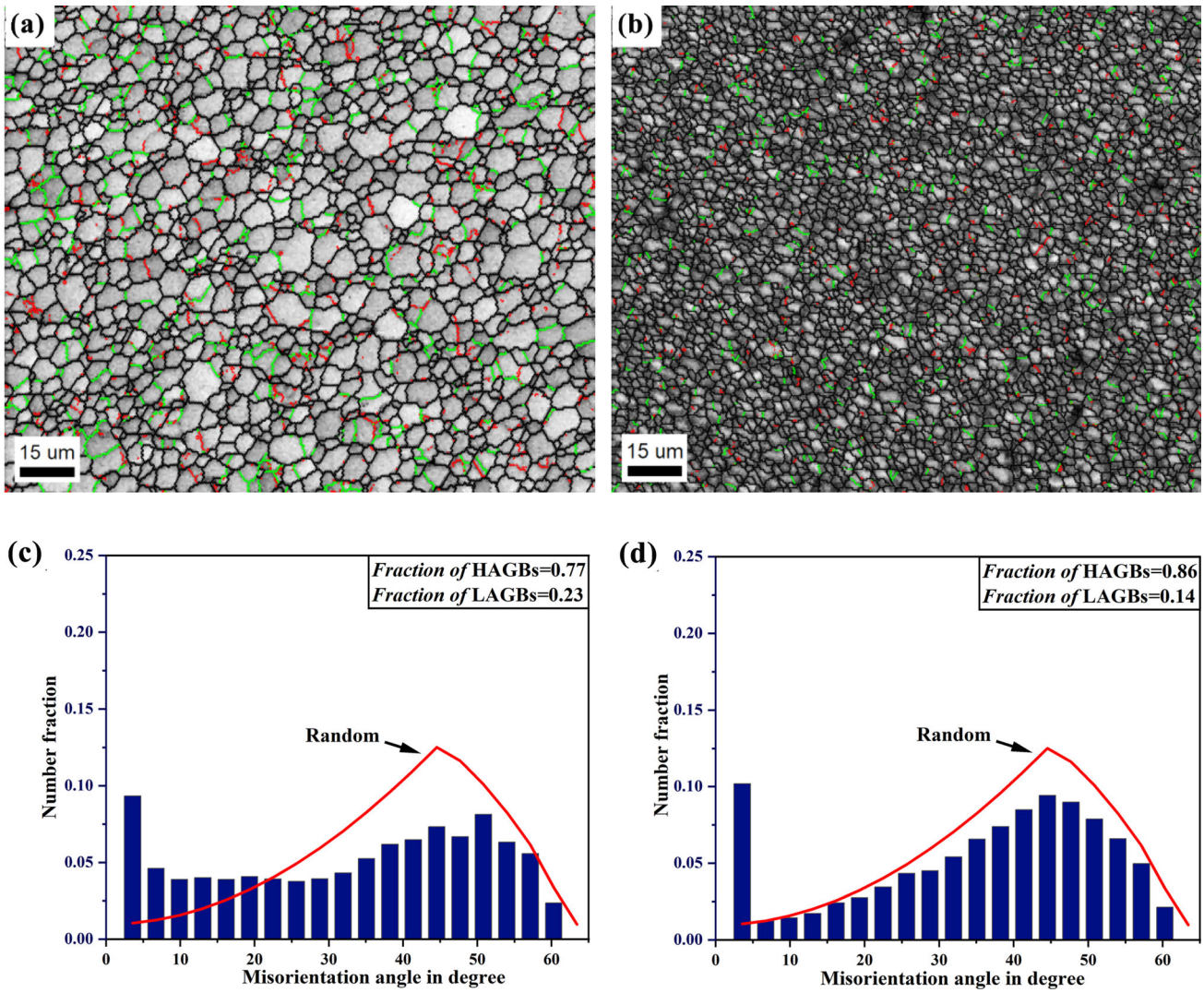

Fig. 7 Grain boundary maps of **a** FSPed sample and **b** AMCs; the corresponding misorientation angle distribution of **a** FSPed sample and **b** AMCs. For the boundary misorientation, red lines: 2–5°, green lines:5–15°, blue lines: > 15°

angle grain boundaries is transformed from classical nucleation and growth during DDRX, whereas the characteristic of GDRX is the formation of serrated grains derived from the impingement of elongated grain boundaries [26, 27]. MDRX implicates the continuation of DRV with the company of stored-strain energy [26]. Figure 7 shows the maps of grain boundary and the corresponding misorientation angle distribution obtained from EBSD of FSPed samples and AMCs. A certain amount of subgrain boundaries (red lines) and low angle grain boundaries (green lines) can be found in the vicinity of the high angle grain boundaries (black lines). This is due to the fact that during the FSP process, the material undergoes both high temperature and intense plastic deformation. However, Al possesses a high stacking fault energy (166 mJ m^{-2}), leading to a rapid increase and annihilation in dislocations with the increase in flow stress, and dynamic recovery occurs. During the recovery process, dislocation is rearranged to form subgrain boundaries. At dynamic equilibrium, the subgrain boundaries continuously absorb dislocations and merge, transforming into low angle grain boundaries. Therefore, when the subgrain size reaches a critical grain size, continuous dynamic recrystallization occurs. In the meantime, the subgrain rotates slowly and the misorientation increases, transforming from a low angle grain boundary to a high angle grain boundary. It is noteworthy that the FSPed sample and AMCs possess similar misorientation angle distribution, both with a random distribution for cubic polycrystals. The ratio of high angle grain boundary in AMCs is about 87%, while that in FSPed sample is about 77%, suggesting that the addition of xGnPs is beneficial to the formation of more sufficient DRX structures.

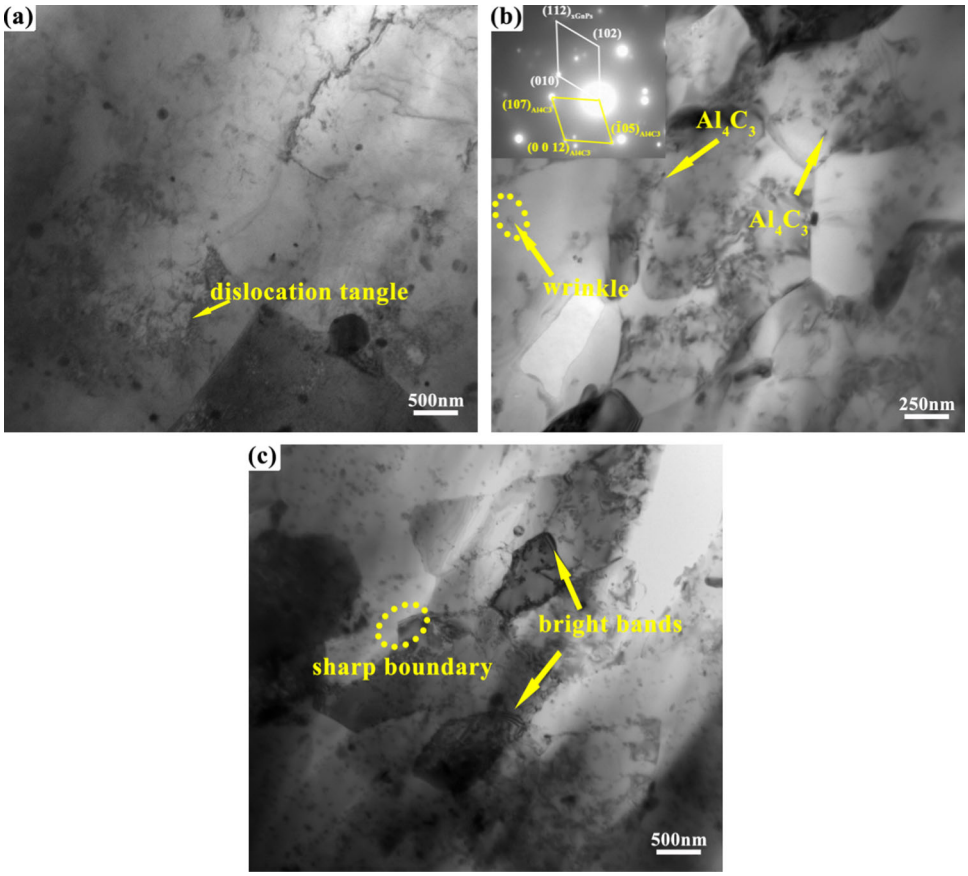

Fig. 8 Bright field TEM images from **a** FSPed sample, **b** and **c** AMCs

There are many dislocations found in the TEM image of the FSPed sample, along with the dislocation cell structures and dislocation tangle observed near grain boundaries, as shown in Fig. 8a. Figure 8b shows that dislocations and cell structures are weakened prominently within AMCs, and the equiaxed grains are significantly increased. The distribution of fine xGnPs is relatively uniform, and there are winkles between xGnPs and matrix, which not only expands the contact area between them, but also facilitates excellent interfacial bonding, with no obvious micropore defects observed. Additionally, some dark features at the edges of the xGnPs indicate the formation of new phases due to the solid-state chemical reaction between the xGnPs and Al during processing to form the Al_4C_3. In accordance with the relevant literature [28], it is known that the Al_4C_3 phase is a typical interfacial reaction product in Al/C composites, and the Gibbs free energy of this reaction is far less than 0 in the temperature range of FSP [21], which is indicative of a spontaneous reaction. Figure 8b shows that Al_4C_3 preferentially nucleates at the open edges of xGnPs rather than at the basal plane, suggesting that Al_4C_3 nucleation is heterogeneous and predominately at defect sites. It is due to the fact that during the FSP, the aluminum matrix undergoes severe plastic deformation while the xGnPs are subjected to friction, crushing and stirring, leading to the breaking of the xGnPs into smaller fragments. The process is conducive to the formation of excellent physical contact between xGnPs and the aluminum matrix, facilitating the formation of bonding between them. Simultaneously, the breakage of C–C bonds at the edges of abundant xGnPs causes the appearance of more active C atoms, giving rise to the open edges of xGnPs are more reactive than the basal planes. As a result, the Al_4C_3 phase was found at the xGnPs edge, while that was not detected at the basal planes.

In Fig. 8c, it is observed that there is a high diffraction contrast between many subgrain boundaries and some bright bands around them, which results from the continuous absorption of lattice dislocations by subgrain boundaries to form long-range stress field and the sharp grain boundaries between adjacent subgrains. Therefore, it is confirmed that the misorientation across these grain boundaries is close to high angle. However, there are no dislocations found in the ultra-fine grains, with sharp and clear grain boundaries. Apparently, these findings are consistent with the characteristics of CDRX. Therefore, it is considered that both CDRX and DDRX occur in both specimens during the FSP process. However, it is probably due to the higher temperature arising from FSP that few features of GDRX and MDRX were found. Not only the effect of DRX generated from

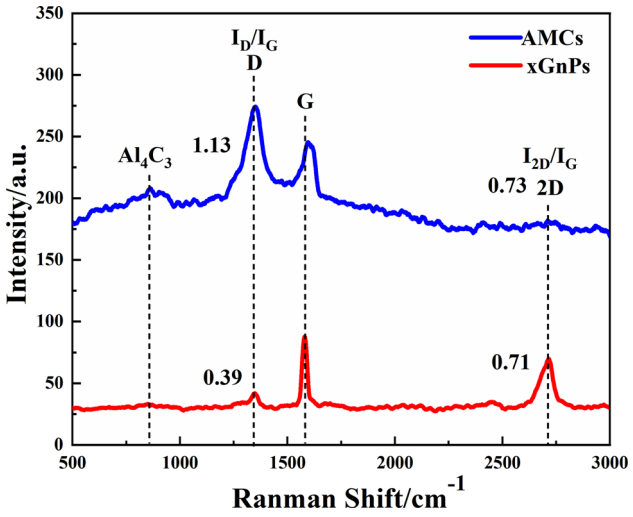

Fig. 9 Raman spectra of nano-graphite powder and AMCs

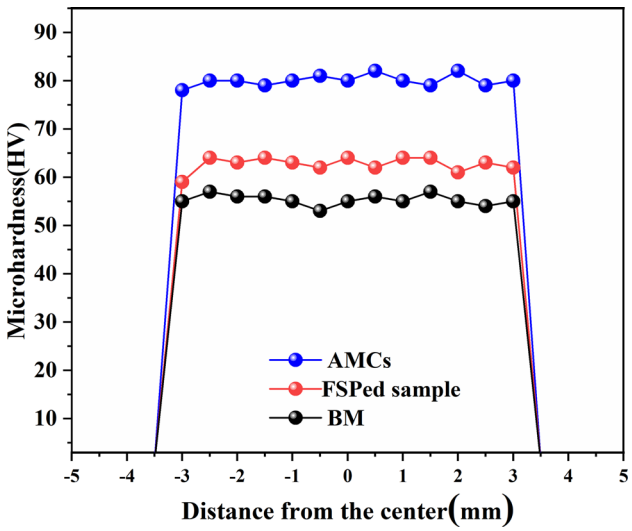

Fig. 10 Microhardness profile of all the samples

FSP but also the high densities of geometrically necessary dislocations formed with the addition of xGnPs that accommodate the strain incompatibility during FSP result in the grain size refiner than FSPed sample by enhancing the nucleation rate during processing. Additionally, in terms of the particulate-stimulated nucleation (PSN) mechanism, the clusters of xGnPs and the size higher than 1 μm could provide preferential nucleation sites for the generation of new grains [29, 30]. On the other hand, in terms of the Zener–Holloman mechanism, the incorporation of xGnPs also can pin grain boundaries [31], which impedes the migration of grain boundaries. Hence, the grain size of AMCs is finer than that of FSPed with the assistance of these two mechanisms simultaneously.

Figure 9 shows the Raman spectra of the AMCs and the xGnPs. The intense peaks in the figure appear at around 1350, 1580 and 2700 cm^{-1}, corresponding to the damage-band (D-band), graphite-band (G-band) and 2D band, respectively. In general, the intensity ratio of D-band to G-band (I_D/I_G) is utilized to estimate the microstructure damage of xGnPs. It can be seen from the graph that there is not a distinct D-peak for the spectra of xGnPs, indicating that its crystal structure is relatively intact. The D-peak is obvious in AMCs, and $I_D/I_G = 1.13$, indicating an increase in lattice defects and a massive reduction in the flake diameter of xGnPs during the FSP process, as further evidenced by Fig. 8b. In addition, the G band in AMCs shifted to a higher value, which is due to the diffusion of Al atoms into the graphite layer under the effect of the severe plastic deformation and high temperature during the FSP process, resulting in the distortion to the SP^2 bond structure and the noticeable peak of Al_4C_3 at 868 cm^{-1}, which further demonstrates the existence of nano-Al_4C_3 in the prepared composites. The value of I_{2D}/I_G is generally employed to evaluate the number of nano-graphite layers, with higher ratios implying higher dispersion. The ratio of I_{2D} to I_G in AMCs is slightly higher than that of xGnPs, demonstrating that there is no large-scale agglomeration within the AMCs. Also, xGnPs are exfoliated during FSP processing.

3.4 Mechanical Properties

Figure 10 shows the microhardness profiles for all the samples along the cross section. The result suggests that the average hardness of BM is about 55HV, while the value of the FSPed sample is about 64HV, which is slightly higher than BM. The main contributors to enhancing the hardness of FSPed sample are grain refinement and the homogenization of precipitates. The hardness was increased to 80HV in AMCs with the addition of xGnPs. Meantime, the hardness distribution curve fluctuates gently, confirming a relatively homogeneous distribution of the reinforcements in the AMCs. It also reflects the effect of grain refinement due to the variation in preferred orientation.

Figure 11 presents the engineering stress–strain curves of BM, FSPed samples and AMCs. The tensile strength, yield strength, and elongation of all the samples were determined according to the tensile test. The main performance parameters measured after tensile examination for the three specimens are shown in Table 3. Compared with BM, both yield strength and tensile strength of FSPed sample and AMCs were enhanced dramatically, despite a decrease in elongation. In general, there are four main strengthening mechanisms contributing to the improved yield strength of AMCs: (i) grain refinement, (ii) dislocation strengthening owing to the coefficient of thermal expansion mismatch between xGnPs and aluminum during the temperature from processing down to the ambient temperature, (iii) interface

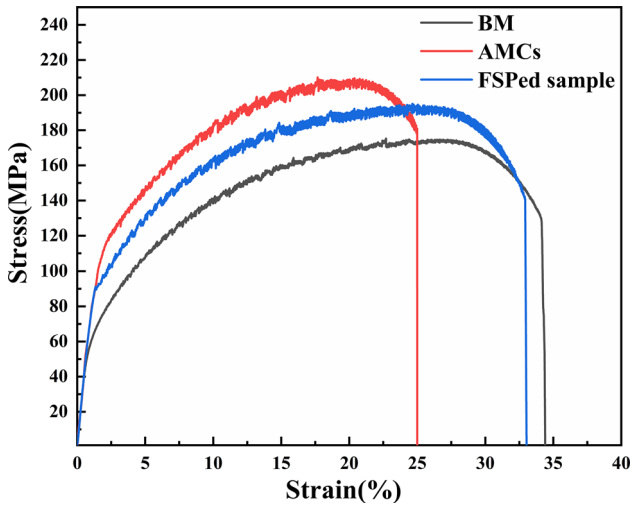

Fig. 11 Stress–strain curves of BM, FSPed sample sand AMCs

Table 3 Tensile properties of BM, FSPed sample and AMCs

Specimen	Tensile strength (MPa)	Yield strength (MPa)	Elongation (%)
BM	175	65	34.17
FSPed sample	195	93	32.91
AMCs	210	110	24.70

load transfer capacity of xGnPs and (iv) Orowan strengthening. The presence of xGnPs at grain boundaries and within the grains contributes to restricting dislocation glide, which increases the probability of dislocation pile-up. The effect of wrapping and pinning related with xGnPs against the grain also impedes the grain growth during FSP, causing finer grain structure formed as a result of DRX, as shown in Figs. 6a and 8b. The strengthening effect generated from grain refinement could be calculated utilizing the Hall–Petch formula as follows [32]:

$$\sigma_y = \sigma_0 + \frac{k_y}{\sqrt{d}} \tag{2}$$

where d represents the average grain size (3.2 μm), σ_y indicates the yield strength, σ_0 denotes the lattice frictional stress (~ 45 MPa for Al–Mg alloy), and k_y refers to a proportional constant depending upon the materials utilized (~ 74 MPa $\mu m^{0.5}$) [33]. Consequently, the yield strength is calculated to be approximately 86.37 MPa due to grain refinement. The thermal mismatch stress would be generated during the FSP process as a result of the large difference in coefficient of thermal expansion between xGnPs (2×10^{-6} K^{-1}) and aluminum (23.6×10^{-6} K^{-1}). Accordingly, there would be more thermal mismatch dislocations formed to alleviate the stresses in the matrix, leading to an increase in dislocation density. Nevertheless, for sub-micron strengthening phase, the thermal mismatch resulting from the difference in expansion of thermal coefficient tends to be mitigated by element diffusion and atom relaxation, resulting in a significant decrease in dislocation density [34]. Herein, the thickness of nanographite is only a few nanometers, and the flake diameter is dozens of nanometers after FSP. Consequently, the dislocation strengthening effect can be ignored. It could be observed that the dispersion of the xGnPs is homogenous inside the grain and Al_4C_3 formed in situ, as shown in the TEM image of Fig. 8b. The formation of this nano-phase is conductive to improving the interfacial load transfer capacity. The following Zener equation [31] could be applied to evaluate the pinning effect of xGnPs.

$$P_z = \frac{3F_V\gamma_\beta}{d} \tag{3}$$

where, F_V is the volume fraction of xGnPs, d is the mean diameter of xGnPs, γ_β is the energy of grain boundaries for base metal, and P_z stands for the induced pinning pressure [31]. It could be found from the above equation that the pinning pressure is inversely proportional to the size of the xGnPs and positively proportional to the volume fraction. Accordingly, the xGnPs as well as in situ formed nano-Al_4C_3 at the grain boundaries are beneficial to inhibiting grain boundary migration more effectively, as shown in Fig. 8b, which leads to Orowan strengthening effect, facilitating the improvement of mechanical performance of AMCs.

3.5 Fractography

Figure 12 depicts the FE-SEM fracture surface of all the samples. According to Fig. 12a, numerous larger dimples and voids exist in BM, demonstrating the typical ductile fracture. The features about ductile fracture are also found in the FSPed sample (Fig. 12b). For example, there is bimodal distribution by means of smaller voids around the larger dimples originated from grain refinement after FSP. The fracture surface for AMCs suggests neither the typical features of ductile nor those of brittle fracture, implicating the mixed characteristics of ductile–brittle failure. As shown in Fig. 12c and d, the dimples on the fracture surface of AMCs are obviously smaller, and small planes appear locally, which is similar to the quasi-cleavage fracture feature. During tensile loading, the dislocation slip was hindered by the reinforcement, creating a stress concentration there, leading to the nucleation of voids around the reinforcement. Subsequently, the coalescence of voids and growth with the increase in loading caused the occurrence of failure. There were also some grain boundaries and triple junctions facilitating crack nucleation. Then, the crack propagated along the weakest neighbor grains in

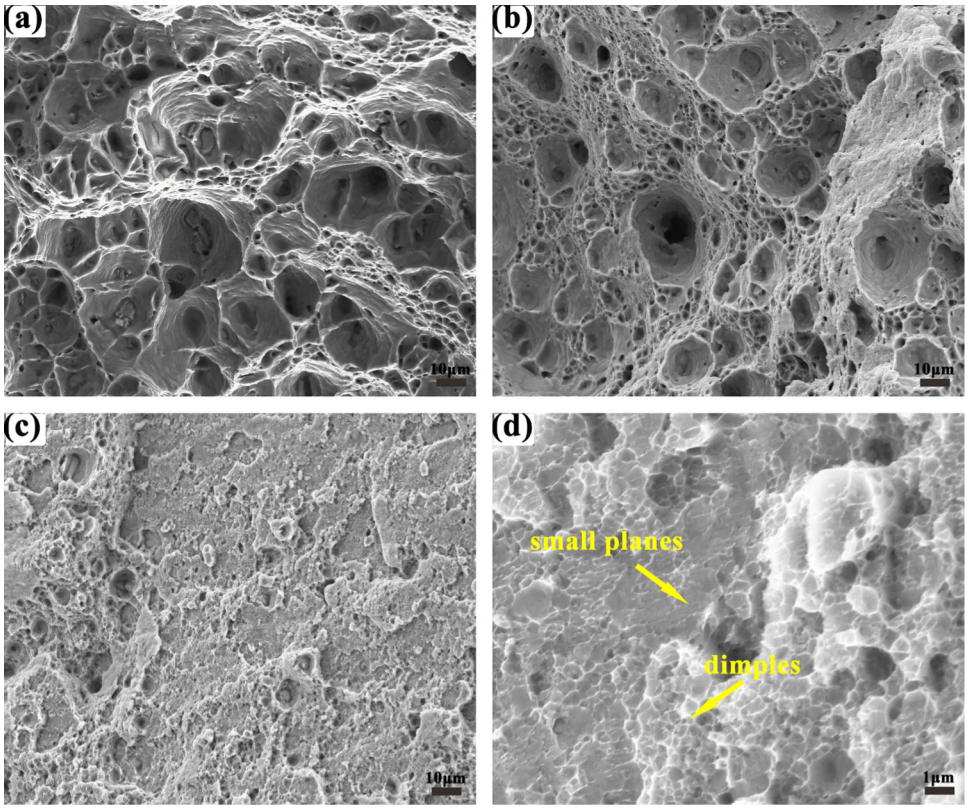

Fig. 12 Fracture surface of (**a**) BM, **b** FSPed sample, **c** AMCs and **d** AMCs at high magnification

the AMCs during tensile test. On the one hand, the xGnPs as the pinning points improved the strength by changing the direction of crack propagation, retarding the occurrence of fracture. On the other hand, the pull-out of xGnPs occurring simultaneously with the interruption effect of the xGnPs on dislocation slip is also responsible for the increase in AMCs strength.

4 Conclusions

In the present study, the effect of xGnPs on the microstructure and mechanical performance of AMCs was investigated, while the strengthening mechanisms were discussed. The main conclusions drawn from the investigation are summarized below:

(1) The Al/xGnPs composites are successfully synthesized using friction stir processing with a uniform distribution of xGnPs. FSP and the incorporation of xGnPs resulted in the preferred orientation of the BM transformed from < 200 > to < 111 > , < 220 > and < 311 > , resulting in the formation of ultra-fine grained structure and the improvement of mechanical performance for AMCs.

(2) The addition of xGnPs not only facilitated the formation of more crystal nucleus by particle stimulated nucleation during DRX, but also activated the Zener–Holloman effect to impede the growth of grain, leading to the generation of fine equiaxed crystals with an average grain size of approximately 3.2 μm and increasing the ratio of high angle grain boundaries in AMCs.

(3) The Al_4C_3 was formed at the edge of graphite sheet as a result of xGnPs reacting with Al matrix during the FSP process. Besides, combined with the action of fine grain strengthening, the hardness, yield strength and ultimate tensile strength of the AMCs reached 80 HV, 110 and 210 MPa, respectively. The tensile fracture of BM and FSPed sample is typical ductile fracture, whereas that of AMCs indicates the characteristics of ductile–brittle mixed fracture.

Acknowledgements The authors sincerely thank Changchun University of Technology, Key Laboratory of Advanced Structural Materials of Ministry of Education for providing the necessary facilities to this work.

References

1. Gupta, M.K.: Analysis of tribological behavior of Al/Gr/MoS 2 surface composite fabricated by friction stir process. Carbon Lett. **30**, 399–408 (2020)
2. Jain, V.K.S.; Varghese, J.; Muthukumaran, S.: Effect of first and second passes on microstructure and wear properties of titanium

dioxide-reinforced aluminum surface composite via friction stir processing. Arab. J. Sci. Eng. **44**, 949–957 (2019)
3. Mehrian, S. M.; Rahsepar, M.; Khodabakhshi, F.; Gerlich, A.: Effects of friction stir processing on the microstructure, mechanical and corrosion behaviors of an aluminum-magnesium alloy. Surf. Coat. Technol. (405) 126647 (2021).
4. Maji, P.; Nath, R.K.; Paul, P.; Meitei, R.; Ghosh, S.K.: Effect of processing speed on wear and corrosion behavior of novel MoS 2 and CeO 2 reinforced hybrid aluminum matrix composites fabricated by friction stir processing. J. Manuf. Process **69**, 1–11 (2021)
5. Yang, X.; Zhang, H.; Cheng, B.; Liu, Y.; Yan, Z.; Dong, P.; Wang, W.: Microstructural, Microhardness and tribological analysis of cooling-assisted friction stir processing of high-entropy alloy particles reinforced aluminum alloy surface composites. Surf. Topogr-Metrol (8) 035012 (2020).
6. Kheirkhah, S.; Imani, M.; Aliramezani, R.; Zamani, M.; Kheilnejad, A.: Microstructure, mechanical properties and corrosion resistance of Al6061/BN surface composite prepared by friction stir processing. Surf. Topogr-Metrol (7) 035002 (2019).
7. Sharma, A.; Narsimhachary, D.; Sharma, V.M.; Sahoo, B.; Paul, J.: Surface modification of Al6061-SiC surface composite through impregnation of graphene, graphite & carbon nanotubes via FSP: a tribological study. Surf. Coat. Technol. **368**, 175–191 (2019)
8. Suryanarayana, C.; Al-Aqeeli, N.: Mechanically alloyed nanocomposites. Prog. Mater. Sci. **58**, 383–502 (2013)
9. Kannan, C.; Ramanujam, R.; Balan, A.: Machinability studies on Al 7075/BN/Al2O3 squeeze cast hybrid nanocomposite under different machining environments. Mater. Manuf. Process. **33**, 587–595 (2018)
10. Khodabakhshi, F.; Simchi, A.: The role of microstructural features on the electrical resistivity and mechanical properties of powder metallurgy Al-SiC-Al2O3 nanocomposites. Mater. Design **130**, 26–36 (2017)
11. Khdair, A.I.; Fathy, A.: Enhanced strength and ductility of Al-SiC nanocomposites synthesized by accumulative roll bonding. J. Mater. Res. Technol. **9**, 478–489 (2020)
12. Mishra, R.S.; Ma, Z.Y.; Charit, I.: Friction stir processing: a novel technique for fabrication of surface composite. Mater. Sci. Eng. A **341**, 307–310 (2003)
13. Khodabakhshi, F.; Arab, S.M.; Švec, P.; Gerlich, A.P.: Fabrication of a new Al-Mg/graphene nanocomposite by multi-pass friction-stir processing: Dispersion, microstructure, stability, and strengthening. Mater. Charact. **132**, 92–107 (2017)
14. Sharma, V.; Prakash, U.; Kumar, B.: Surface composites by friction stir processing: A review. J. Mater. Process. Tech. **224**, 117–134 (2015)
15. Mishra, R.S.; De, P.S.; Kumar, N.: Friction stir welding and processing. Springer International Publishing (2014). https://doi.org/10.1007/978-3-319-07043-8
16. Khodabakhshi, F.; Nosko, M.; Gerlich, A.P.: Dynamic restoration and crystallographic texture of a friction-stir processed Al–Mg–SiC surface nanocomposite. Mater. Sci. Technol. **34**(14), 1773–1791 (2018)
17. Liu, Y.; Chen, G.; Zhang, H.; Yang, C.; Zhang, S.; Liu, Q.; Zhou, M.; Shi, Q.: In situ exfoliation of graphite for fabrication of graphene/aluminum composites by friction stir processing. Mater. Lett. (301) 130280 (2021).
18. Dixit, S.; Mahata, A.; Mahapatra, D.R.; Kailas, S.V.; Chattopadhyay, K.: Multi-layer graphene reinforced aluminum–manufacturing of high strength composite by friction stir alloying. Compos. B Eng. **136**, 63–71 (2018)
19. Jain, V.K.S.; Yazar, K.; Muthukumaran, S.: Development and characterization of Al5083-CNTs/SiC composites via friction stir processing. J. Alloys Compd. **798**, 82–92 (2019)
20. Sharma, A.; Fujii, H.; Paul, J.: Influence of reinforcement incorporation approach on mechanical and tribological properties of AA6061-CNT nanocomposite fabricated via FSP. J. Manuf. Process **59**, 604–620 (2020)
21. Khodabakhshi, F.; Gerlich, A.; Švec, P.: Reactive friction-stir processing of an Al-Mg alloy with introducing multi-walled carbon nano-tubes (MW-CNTs): microstructural characteristics and mechanical properties. Mater. Charact. **131**, 359–373 (2017)
22. Fustes, J.; Gomes, A.; da Silva Pereira, M.: Electrodeposition of Zn–TiO 2 nanocomposite films—effect of bath composition. J. Solid State Electrochem. (12) 1435–1443 (2008).
23. Berube, L. P.; L'Espérance, G.: A quantitative method of determining the degree of texture of zinc electrodeposits. J. Electrochem. Soc. (136) 2314 (1989).
24. Nasir, E.M.: Texture coefficient and conductivity dependence on the annealing and thicknesses of thin CdS films. Int. Rev. Phys. **7**(1), 22–25 (2013)
25. Sakai, T.; Belyakov, A.; Kaibyshev, R.; Miura, H.; Jonas, J.J.: Dynamic and post-dynamic recrystallization under hot, cold and severe plastic deformation conditions. Prog. Mater. Sci. **60**, 130–207 (2014)
26. McNelley, T.; Swaminathan, S.; Su, J.: Recrystallization mechanisms during friction stir welding/processing of aluminum alloys. Scr. Mater. **58**, 349–354 (2008)
27. Khodabakhshi, F.; Simchi, A.; Kokabi, A.; Gerlich, A.; Nosko, M.: Effects of stored strain energy on restoration mechanisms and texture components in an aluminum–magnesium alloy prepared by friction stir processing. Mater. Sci. Eng. A **642**, 204–214 (2015)
28. Jiang, Y.; Tan, Z.; Fan, G.; Zhang, Z.; Xiong, D.-B.; Guo, Q.; Li, Z.; Zhang, D.: Nucleation and growth mechanisms of interfacial carbide in graphene nanosheet/Al composites. Carbon **161**, 17–24 (2020)
29. Khodabakhshi, F.; Simchi, A.; Kokabi, A.; Nosko, M.; Simanĉik, F.; Švec, P.: Microstructure and texture development during friction stir processing of Al–Mg alloy sheets with TiO2 nanoparticles. Mater. Sci. Eng. A **605**, 108–118 (2014)
30. Khodabakhshi, F.; Simchi, A.; Kokabi, A.; Švec, P.; Simančík, F.; Gerlich, A.: Effects of nanometric inclusions on the microstructural characteristics and strengthening of a friction-stir processed aluminum–magnesium alloy. Mater. Sci. Eng. A **642**, 215–229 (2015)
31. Ammouri, A.; Kridli, G.; Ayoub, G.; Hamade, R.: Relating grain size to the Zener-Hollomon parameter for twin-roll-cast AZ31B alloy refined by friction stir processing. J. Mater. Process. Tech. **222**, 301–306 (2015)
32. Hansen, N.: Hall-Petch relation and boundary strengthening. Scr. Mater. **51**, 801–806 (2004)
33. Khodabakhshi, F.; Gerlich, A.; Simchi, A.; Kokabi, A.: Cryogenic friction-stir processing of ultrafine-grained Al–Mg–TiO2 nanocomposites. Mater. Sci. Eng. A **620**, 471–482 (2015)
34. Kim, C.; Lee, J.; Plichta, M.: Plastic relaxation of thermoelastic stress in aluminum/ceramic composites. Metall. Trans. A **21**, 673–682 (1990)